Synthesis and photoluminescence properties of Mn2+ doped ZnCN2 phosphors

Erwan Leysour de Rohello, Francesco Bour, Yan Suffren, Odile Merdrignac-Conanec, Olivier Guillou, François Cheviré

Synthesis and photoluminescence properties of Mn^{2+} doped $ZnCN_2$ phosphors

Erwan Leysour de Rohello, Francesco Bour, Yan Suffren, Odile Merdrignac-Conanec, Olivier Guillou, François Cheviré*

Univ Rennes 1, INSA Rennes, CNRS, ISCR (Institut des Sciences chimiques de Rennes) – UMR 6226, F-35000 Rennes, France

*Corresponding author : francois.chevire@univ-rennes1.fr

Abstract

Mn^{2+} doped $ZnCN_2$ phosphors were synthesized by a solid-state reaction from doped zinc oxalate and carbon nitride under NH_3 atmosphere at 600 °C in only 1 h. The samples were characterized by powder X-ray diffraction, scanning electron microscopy and their diffuse reflectance and luminescence properties were investigated. All pure and well-crystallized Mn^{2+} doped samples exhibit broad orange emission around 585 nm when excited at 270 nm at room temperature corresponding to the $^4T_{1g}(^4G) \rightarrow {}^6A_{1g}(^6S)$ transition. Maximum emission is obtained for Mn^{2+} content of 2 mol% and the emission intensity decreases drastically on the order of 90% between 293 and 385 K. Additionally, the blue luminescence of as-prepared non-doped $ZnCN_2$ is discussed on the basis of the presence of crystal defects.

Keywords: zinc carbodiimide, carbon nitride, luminescence, phosphor, Mn^{2+} activator

1. Introduction

In recent years, inorganic carbodiimide materials with general formula $M_x(NCN)_y$ (M=alkali, alkaline-earth, rare-earth, transition metals or metalloids) have gained increasing attention due to remarkably high thermal and chemical properties, which make them excellent candidates as luminescent host materials. Recently, alkaline-earth and rare-earth carbodiimides compounds have been applied as host materials for Ce^{3+}, Eu^{2+} or Mn^{2+} doping. Some examples are $Gd_2(CN_2)_3:Ce^{3+}$ which produces an amber emission with a maximum of the emission band at approximately 575 nm under 415 nm light excitation [1]. An orange emission between 610 and 620 nm is reported for $SrCN_2:Eu^{2+}$ in response to excitation at 440 nm [2–4]. A longer emission wavelength of 660 nm has been reported for $BaCN_2:Eu^{2+}$ under 365 nm light excitation [5]. Finally, $CaCN_2$ was also studied as a host material for Mn^{2+} where the activator is octahedrally coordinated by nitrogen atoms resulting in an intense bright red emission at 680 nm at room temperature under 270 nm excitation wavelength [6,7].
As part of the family of nitrogenous materials, $ZnCN_2$ have been considered for various applications such as corrosion inhibitor [8], water-oxidation photocatalyst or negative electrode for Li-ion batteries [9,10]. $ZnCN_2$ is so far commonly obtained by aqueous precipitation processes [11,12] and adopts a tetragonal $I\bar{4}2d$ crystal structure which consists of a three-dimensional network of $[ZnN_4]$ tetrahedrons sharing their corners. Let us note that thin films of $ZnCN_2$ have also been produced by CVD [13]. To the best of our knowledge, no investigation has been focused on studying luminescence properties of Mn^{2+} doped $ZnCN_2$, while several doped nitride phosphors where Mn^{2+} is tetrahedrally coordinated have been reported such as $AlN:Mn^{2+}$, $ZnSiN_2:Mn^{2+}$, $MgSiN_2:Mn^{2+}$ or $ZnGeN_2:Mn^{2+}$ [14–17]. Recently, we reported a simple synthetic route for the preparation of highly crystallized Mn^{2+}

doped $CaCN_2$ in only one hour at moderate temperature under NH_3 atmosphere using directly doped calcium carbonate and carbon nitride as precursors [3,7]. The aim of this study is therefore to investigate the synthesis of Mn^{2+} doped $ZnCN_2$ using the synthetic route developed in our previous study. The influence of Mn^{2+} doping concentration on the crystal structure and luminescent properties is investigated. Additionally, the blue luminescence of as-prepared non-doped $ZnCN_2$ is discussed on the basis of the presence of crystal defects.

2. Experimental procedure

2.1. Preparation of Mn^{2+} doped zinc carbodiimides

Powder samples with general formula $Zn_{1-x}Mn_xCN_2$ (x = 0, 0.005, 0.01, 0.02, 0.03, 0.04, 0.05 and 0.1) were synthesized through solid-state reaction from (doped) zinc oxalate and carbon nitride (C_3N_4). 3 g of non-doped or doped zinc oxalate precursors were prepared by co-precipitation method using $Zn(NO_3)_2{\cdot}6H_2O$ (Sigma Aldrich, 98%), $MnCl_2{\cdot}4H_2O$ (Alfa Aesar, 99%) and $(NH_4)_2C_2O_4{\cdot}H_2O$ (Alfa Aesar, ≥99%) as raw materials. Appropriate amounts of zinc nitrate and manganese chloride were dissolved in 100 mL of deionized water until obtaining a homogeneous solution, which was then added drop-wise into a 150 mL ammonium oxalate solution (molar ratio C_2O_4/Zn = 1.5) under vigorous stirring. A white precipitate was formed and separated from the solution by centrifugation at 4000 rpm for 5 min with intermediate rinsing with deionized water (x3) then ethanol (x2) in order to remove any unprecipitated impurities. Finally, the resulting precipitate was dried in an oven at 80 °C overnight to obtain the (doped) zinc oxalate powder precursor. Carbon nitride (C_3N_4) powder was synthesized by heating melamine in a muffle furnace. In a typical synthesis run, 15 g of melamine (Aldrich, 99%) was placed into an enclosed alumina crucible and then heated up to 550 °C for 5 h with a heating rate of 3 °C min^{-1}. The as-obtained yellow product was collected and ground into powder for further use. All zinc carbodiimide samples have been synthesized according to the following procedure. 500 mg of non-doped or doped zinc oxalate was thoroughly mixed with 1 g of carbon nitride in an agate mortar. The resulting mixture was placed in an alumina crucible and loaded in a tubular furnace under nitrogen flow (N_2). The furnace was purged during 15 min before switching to ammonia (NH_3) with a flow rate of 12 L h^{-1}. Then the mixture was heated at 600 °C for 1 h with a heating rate of 10 °C min^{-1}. Thereafter, the tubular furnace was turned off and allowed to cool down to room temperature. Finally, the resulting white powder was transferred and stored in a glovebox. Let us note that NH_3 atmosphere was necessary to remove carbon residues during the heat treatment.

2.2. Characterizations

X-ray diffraction (XRD) patterns were recorded at room temperature in the 10-90° 2θ range with a step size of 0.0261° and an effective scan time per step of 40 s using a PANalytical X'Pert Pro diffractometer (Cu-L2,L3 radiation, λ = 1.5418 Å, 40 kV,40 mA, PIXcel 1D detector). Data collector and HighScore Plus programs were used, respectively, for recording and analysis of the patterns. The purity of all the prepared powders was systematically checked by XRD. The powder XRD patterns for Rietveld refinements were collected at room temperature in the 5-120° 2θ range with a step size of 0.0131° and an effective scan time per step of 200 s. All calculations were carried out with Fullprof and WinPLOTR programs [18,19]. The pseudo-Voigt profile function was used and the background was approximated by linear interpolation between a set of background points. The lattice parameters were obtained from Rietveld refinements considering the space group $I\bar{4}2d$ (no. 122). Zinc and manganese were considered occupying the same crystallographic site with respective site occupancies calculated from the targeted chemical compositions. The same thermal parameter was applied for all atoms

occupying the zinc site (Wyckoff site: 8*d*) and the site occupancies were not refined. The estimated standard deviations (ESD) were corrected using the Berar and Lelann coefficient calculated from the structure refinement [20,21].

Nitrogen and oxygen contents were determined with a LECO TC-600 Analyzer using the inert gas fusion method in which nitrogen and oxygen contents were measured as N_2 by thermal conductivity and as CO_2 by infrared detection, respectively.

Powders morphology was examined by Scanning Electron Microscopy (SEM) with a JEOL JSM 7100 F equipment (CMEBA, University of Rennes 1) operating at 6 mm working distance with an accelerating voltage of 20 kV. Energy dispersive X-ray spectroscopy (EDS) analyses were performed using a JEOL IT300 microscope operating at 10 mm working distance with an accelerating voltage of 20 kV and a probe current of 7.45 nA. Sample preparation consisted in powder deposition on a carbon tape followed by metallization with gold.

Thermogravimetric analysis (TGA) and Differential Scanning Calorimetry (DSC) measurements were performed with a NETZSCH STA 449 F3 Jupiter analyzer equipped with a Proteus Analysis software. The analyses were performed in alumina crucible under simulated air (N_2/O_2 – 80 vol%/20 vol%) and under nitrogen (N_2 – 100 vol%) in a temperature range from 20 to 985 °C with a heating rate of 10 °C.min^{-1}.

Diffuse reflectance spectra were collected using a Varian Cary 100 Scan spectrometer equipped with a Varian WinUV software and the integrating sphere Lab-sphere (DRC-CA-30). Experimental data were collected within the 250-800 nm range with a 1 nm step. Band gaps of the materials (E_g) were estimated using the Kubelka-Munk formalism [22].

Solid-state excitation and emission spectra were measured with a Horiba Jobin-Yvon Fluorolog-III fluorimeter equipped with a Xe lamp 450 W and a UV-Vis photomultiplier (Hamamatsu R928, sensitivity 190 - 860 nm). For the measurements recorded above room temperature, the samples were placed in an adequate solid holder then introduced in the F-3004 Jobin-Yvon heating Peltier module (293 – 383 K). Appropriate filters were utilized to remove the laser light, the Rayleigh scattered light and associated harmonics from the emission spectra. All spectra were corrected for the instrumental response function. Luminescence decays were measured directly with the fluorescence spectrometer coupled with an additional TCSPC module (Time-Correlated-Single-Photon-Counting) and a 284 nm pulsed Delta-Diode. Lifetimes are averages of three independent determinations.

3. Results and discussion

3.1. Materials characterization

The XRD patterns of the series of powder samples $Zn_{1-x}Mn_xCN_2$ (x = 0, 0.005, 0.01, 0.02, 0.03, 0.04, 0.05 and 0.1) are displayed in Figure S1. The results show that all the products can be readily indexed as tetragonal phase and identified as $ZnCN_2$ according to the COD card no. 201-1886 [23]. Nevertheless, traces of a secondary phase identified as $MnCN_2$ (SG: $R\bar{3}m$ (n°166), COD card no. 110-0722) were observed in samples with Mn^{2+} doping rates greater than 4 mol% as depicted on the zoomed inset in Figure S1 where the (003) and $(10\bar{2})$ lines of $MnCN_2$ are slightly noticeable at about 18.5° and 33.2°, respectively. The powder diffraction data of the as-prepared samples were analyzed by Rietveld refinement. Details of crystal structure parameters and of the refinement as well as the atomic parameters are listed in Tables 1 and S1. Final Rietveld refinement patterns of the whole series of powders are very similar, so that only the refinement pattern of $Zn_{0.98}Mn_{0.02}CN_2$ is presented in Figure 1.

Table 1. Details of the Rietveld refinement of the $Zn_{1-x}Mn_xCN_2$ samples.

Mn^{2+} (%)	**0**	**0.5**	**1**	**2**	**3**	**4**	**5**	**10**
Space group, *Z*	Tetragonal, $I\bar{4}2d$ (n° 122), 8							
Lattice parameters								
***a* (Å)**	8.8113(4)	8.8122(4)	8.8136(3)	8.8167(3)	8.8174(1)	8.8181(4)	8.8181(4)	8.8169(6)
***c* (Å)**	5.4308(3)	5.4317(3)	5.4326(1)	5.4341(3)	5.4356(2)	5.4363 (3)	5.4363(3)	5.4355 (5)
Volume (Å³)	421.65(4)	421.81(2)	422.00(3)	422.42(1)	422.60(3)	422.72(3)	422.73(4)	422.54(5)
Figure of merits								
***R_p* (%)**	6.76	6.80	6.69	6.81	6.87	7.35	7.31	9.99
***R_{wp}* (%)**	7.97	7.99	7.66	7.69	7.72	8.06	8.14	10.7
***R_{exp}* (%)**	5.42	5.50	5.53	5.68	5.80	5.94	6.04	7.12
R_{bragg}	1.96	1.89	1.40	1.74	1.57	1.85	1.82	1.75
χ^2	2.16	2.11	1.92	1.83	1.77	1.84	1.79	2.25

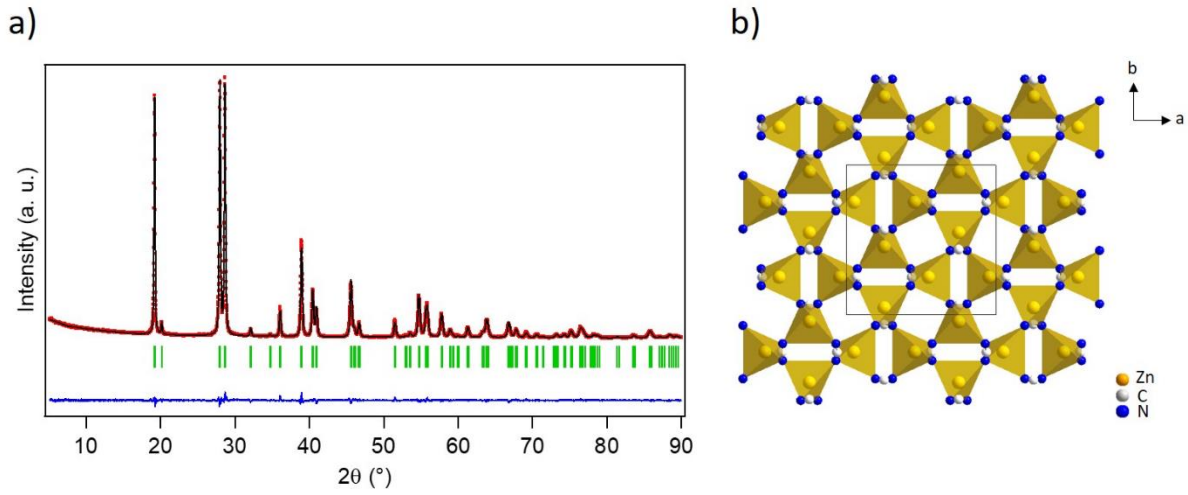

Figure 1. a) Final Rietveld refinement pattern for $Zn_{0.98}Mn_{0.02}CN_2$: observed (red dotted line), calculated (black full line) and difference (blue line) X-ray powder diffraction profiles from the pattern-matching plot obtained with Fullprof. The vertical markers correspond to the position of the Bragg reflections. b) Crystal structure of $ZnCN_2$.

The crystallographic structure of $ZnCN_2$ based on Rietveld refinement is shown in Figure *1*b. It consists of a three-dimensional network of corner sharing [ZnN_4] tetrahedrons so that nitrogen atoms are located in a triangular environment formed by two zinc atoms and one carbon atoms from the [N=C=N] units. The [ZnN_4] tetrahedrons are slightly deformed leading to two Zn-N bond lengths of the order of 1.98 Å and 2.04 Å, respectively. The [N=C=N] pattern is symmetrical with a single C-N bond length of about 1.21 Å but slightly distorted ($\widehat{NCN}$ = 174.1°). For comparison, Becker *et al.* reported identical Zn-N bond lengths and a C-N bond length of 1.22 Å with an N-C-N angle of 176.3° when the zinc carbodiimide was precipitated from aqueous solution of $ZnSO_4$ and $Na_2(CN_2)$ [11]. Let us note here that preliminary tests aimed at obtaining directly $ZnCN_2$:Mn^{2+} by precipitation were not conclusive due to the propensity of Mn^{2+} to precipitate on its own as $Mn(OH)_2$ under the pH conditions necessary to obtain $ZnCN_2$.

Figure 2 shows the evolution of the *a* and *c* unit cell parameters, as well as the *V* cell volume of the samples as a function of the Mn^{2+} doping concentrations. The linear increase of the cell parameters (*a*, *c* and *V*) up to 3 mol% Mn^{2+} concentration confirms the insertion of Mn^{2+} within the structure of the

host material $ZnCN_2$, as it is expected that the average ionic radius increases slightly since the dopant ions ($r_{Mn^{2+}}$ = 0.66 Å) substitute for the Zn^{2+} ions ($r_{Zn^{2+}}$ = 0.60 Å, C.N. = 4) [24]. The lattice parameters values remain thereafter almost constant up to 10 mol% Mn^{2+} doping rate due to the formation of $MnCN_2$ as secondary phase.

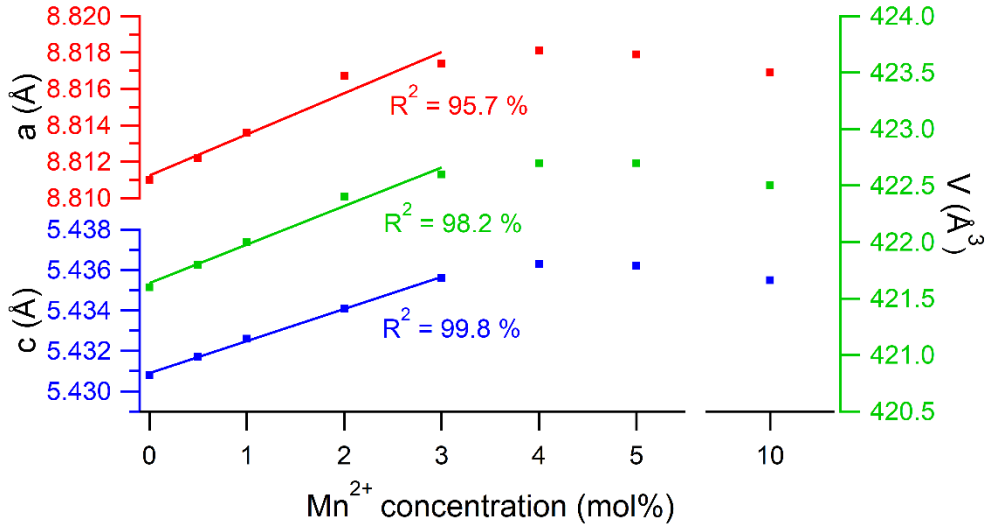

Figure 2. Evolution of the *a*, *c* unit cell parameters and *V* cell volume in $Zn_{1-x}Mn_xCN_2$ samples as a function of Mn^{2+} doping concentration.

SEM images of $ZnCN_2$ and $Zn_{0.98}Mn_{0.02}CN_2$ powders are presented in Figure 3. The latter consist of large agglomerates with sizes up to few micrometers. The agglomerates are composed of rounded shape primary particles whose size is around 100 nm. At high magnification, SEM images show an interconnected microstructure produced by the partial sintering of the particles arising from the heat treatment of 1 h at 600 °C. The porous structure is likely to be inherited from the oxalate precursor grains shape due to the loss of mass during the rapid conversion from $[C_2O_4]^{2-}$ (M = 88.02 g.mol^{-1}) to $[CN_2]^{2-}$ (M = 40.02 g.mol^{-1}) and evolution of oxygen containing gas such as CO_x and H_2O.

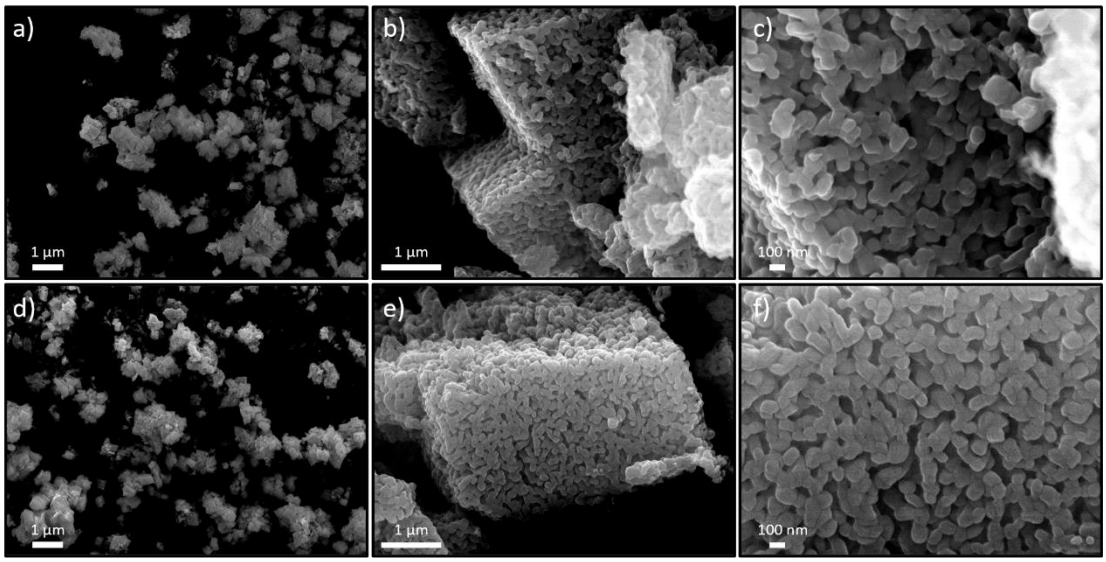

Figure 3. SEM images of (a–c) $ZnCN_2$ and (d–f) $Zn_{0.98}Mn_{0.02}CN_2$.

Elemental analysis was performed on each sample in order to determine the amount of dopant as well as the nitrogen and oxygen contents using EDS and the inert gas fusion techniques, respectively. The elemental analysis data of the as-prepared powders are summarized in Table 2. The obtained

results confirm that the amount of Mn^{2+} is in good agreement with the targeted ones while nitrogen contents are in line with calculated values within experimental errors. The oxygen amount in each sample did not exceed 1 %wt.

Table 2. Chemical composition and Mn^{2+} content of $Zn_{1-x}Mn_xCN_2$ samples.

	Zn at%	Mn at%	N_{exp} wt%	N_{calc} wt%	ΔN %*	O wt%
$ZnCN_2$	100	-	26.69	26.57	0.45	0.30
$Zn_{0.995}Mn_{0.005}CN_2$	99.45	0.55	27.54	26.58	3.61	0.40
$Zn_{0.99}Mn_{0.01}CN_2$	98.72	1.28	27.00	26.60	1.50	0.57
$Zn_{0.98}Mn_{0.02}CN_2$	98.03	1.97	27.63	26.62	3.79	0.32
$Zn_{0.97}Mn_{0.03}CN_2$	96.78	3.22	26.72	26.64	0.30	0.39
$Zn_{0.96}Mn_{0.04}CN_2$	96.11	3.89	27.51	26.67	3.15	0.37
$Zn_{0.95}Mn_{0.05}CN_2$	94.72	5.28	27.68	26.70	3.67	0.36
$Zn_{0.90}Mn_{0.10}CN_2$	89.59	10.41	26.60	26.83	0.86	0.91

* Deviation of the experimental nitrogen rate from the theoretical value

In addition, thermal analyses (TGA – DSC) were conducted in order to characterize the stability of $ZnCN_2$ sample under simulated air and nitrogen atmospheres as shown in Figure 4. Under air, the TGA signal decreases from 558 °C and reveals a maximum experimental weight loss (-23.55%) associated with an exothermic phenomenon corresponding to the oxidation of $ZnCN_2$ into ZnO (theoretical weight loss: -22.76%). Under nitrogen, the TGA signals shows a mass loss starting at 744°C and continuing above 985°C associated to the slow decomposition of the compound due to zinc sublimation at high temperature. According to Morita *et al.* [12], who observed a similar thermal behavior of $ZnCN_2$ under nitrogen atmosphere, the following decomposition reaction occurs above 800°C: $2\ ZnCN_2 \rightarrow 2\ Zn + (CN)_2\uparrow \rightarrow + N_2\uparrow$ rapidly followed by the endothermic vaporization of zinc above 900°C associated with an increase in the weight loss rate.

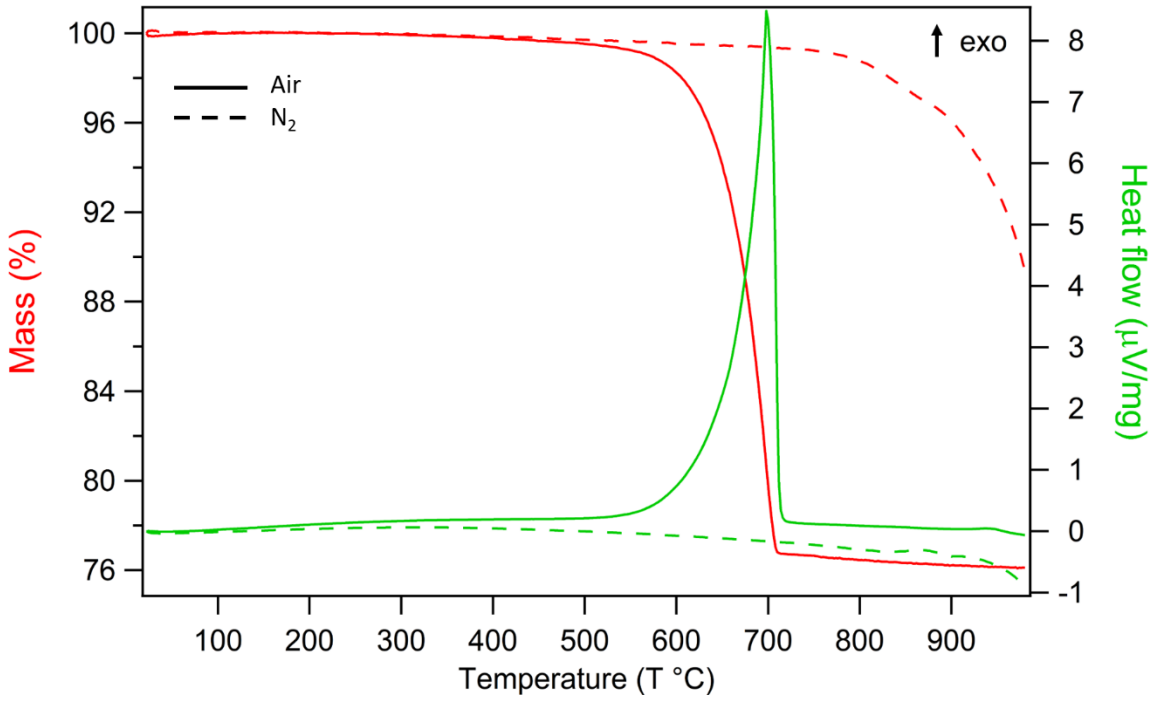

Figure 4. TGA (red) and DSC (green) curves of $ZnCN_2$ under air (full curves) and nitrogen (dashed curves).

3.2. Diffuse reflection spectra

Figure 5 shows the diffuse reflection spectra of non-doped and Mn^{2+}-doped $ZnCN_2$ samples. The non-doped sample presents a double absorption edge. The first one located at about 270 nm with an estimated band gap of about 4.8 eV is essentially attributed to the valence-to-conduction band transitions of the $ZnCN_2$ host lattice likely to occur between the *2p*(N) states at the top of the valence band and the *4s*(Zn) states at the bottom of the conduction band [12]. The second one positioned around 375 nm is attributed to *2p*(O) states within the bandgap associated to the presence of oxygen defects in the lattice as it corresponds to energy gap around 3.2 eV commonly reported in ZnO for electronic transitions between *2p*(O) and *4s*(Zn) states [25]. For Mn^{2+}-doped samples, an additional absorption band can be observed around 260-280 nm that shifts to higher wavelengths with increasing Mn^{2+} content. This band can be ascribed to the presence of *3d*(Mn) states within the band gap of $ZnCN_2$ as they are expected at a lower energy than the *4s*(Zn) states. The daylight color of doped samples shows white to light-brown color, varying with Mn^{2+} doping rate as a result of the absorption by Mn^{2+} ion in the visible range ascribed to the 3d-3d electronic transitions.

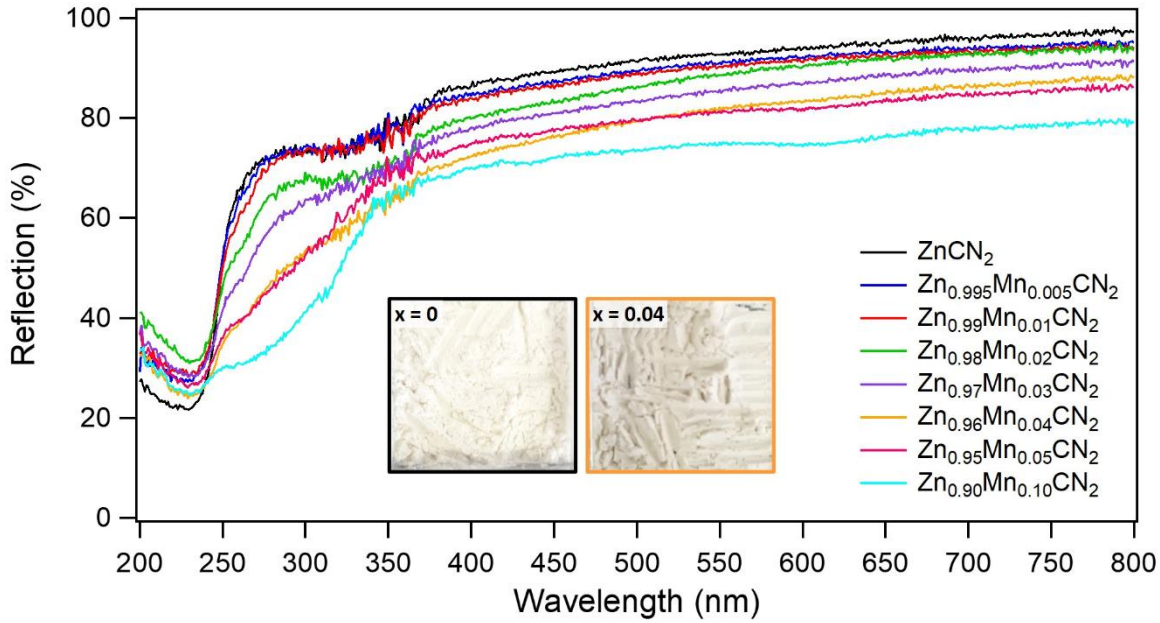

Figure 5. Solid-state diffuse reflection spectra of non-doped and Mn^{2+}-doped $ZnCN_2$ samples at room temperature. In inset: Appearance of $ZnCN_2$ (left picture) and $Zn_{0.96}Mn_{0.04}CN_2$ (right picture) powders in daylight.

3.3. Photoluminescence studies of non-doped and Mn^{2+}-doped $ZnCN_2$ samples

3.3.1 Photoluminescence properties of non-doped $ZnCN_2$ sample

Figure 6 presents the luminescence spectra of the $ZnCN_2$ sample at room temperature, the Commission Internationale de l'Eclairage (CIE) chromaticity diagram [26], chromaticity coordinates and a photograph under 254 nm UV lamp. By monitoring the emission at 440 nm, the sample shows two excitation bands. The first one is the most intense and originates from host lattice excitation around 270 nm. The second one, less intense, centered at 330 nm (3.75 eV) is attributed to the presence of defects within the lattice, in good correlation with the absorption band observed on the diffuse reflectance spectrum. Under excitation at 270 nm, the emission spectrum shows a broad emission band centered at 440 nm (2.81 eV) with a shoulder at 525 nm (2.36 eV). The full-width at half-maximum (FWHM) is estimated around 170 nm and the CIE chromaticity coordinates are

(x = 0.232, y = 0.264). The presence of such shoulder indicates that the observed emission band is probably the sum of at least two contributions. Lower energy excitation (λ_{exc} = 330 nm) results in a flattening of the emission band attributed to a much greater decrease in the component at 440 nm compared to that at about 525 nm.

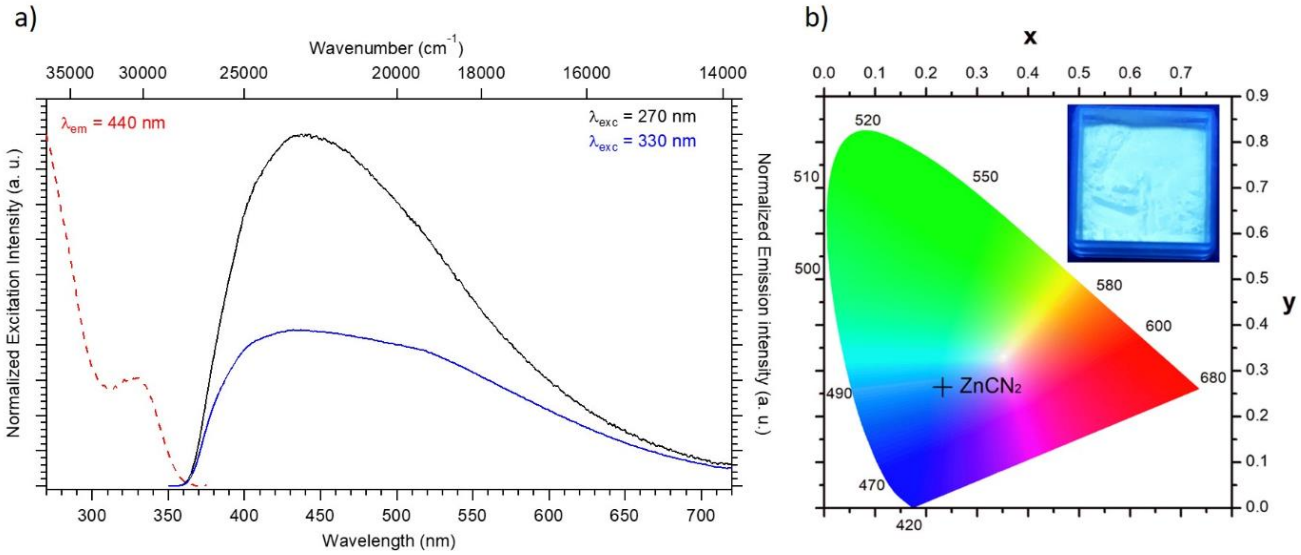

Figure 6. a) Excitation (λ_{em} = 440 nm, red curve) and emission (λ_{exc} = 270 and 330 nm, black and blue curves, respectively) spectra of $ZnCN_2$ at room temperature. b) The CIE chromaticity diagram, chromaticity coordinates, and picture under 254 nm UV lamp.

Such large emission band profile with shoulders is generally observed in semiconductors such as ZnO or ZnS where localized defects (e.g. vacancies or interstitial atoms) are at the origin of the photoluminescence [27–29]. However, as the photoluminescence properties of $ZnCN_2$ are reported here for the first time, it is difficult to attribute their origin with certitude. Nevertheless, by analogy with the fluorescence mechanisms reported in the literature for ZnO, we can make several hypotheses on the nature of those occurring in $ZnCN_2$ (Figure 7).

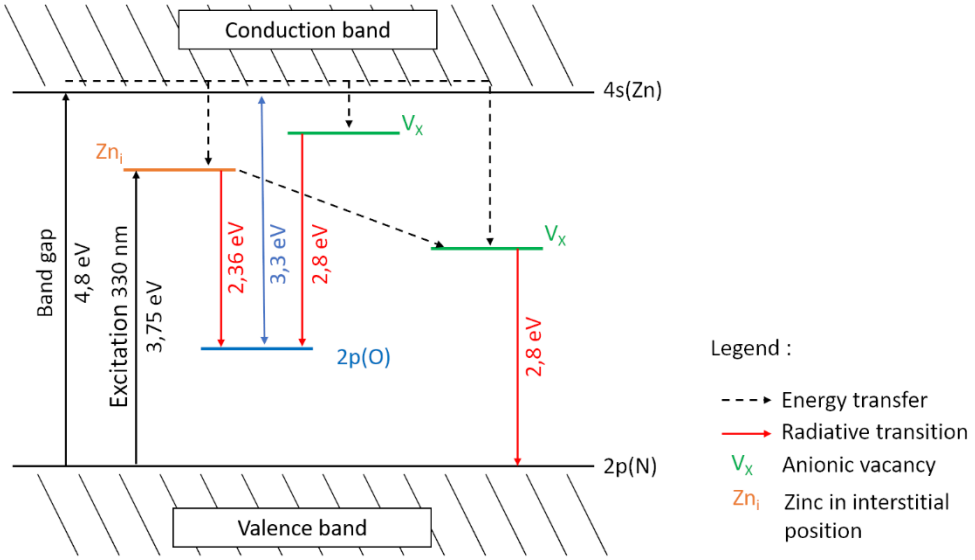

Figure 7. Proposed fluorescence mechanisms for $ZnCN_2$ (Note that the nature of the defects (V_x and Zn_i) associated with the energy levels in the diagram is given only as an example).

The top of valence band (VB) and the conduction band (CB), respectively associated with *2p*(N) and *4s*(Zn) orbitals, are separated by an energy of 4.8 eV, corresponding to the optical gap measured for $ZnCN_2$. The *2p*(O) states are placed at 3.3 eV from the bottom of the conduction band by analogy to the optical gap usually reported in ZnO and based on the result of the diffuse reflectance analysis [25]. The occurrence of two absorption bands on the excitation spectrum allows for two possible excitation paths to be defined. The first path corresponds to the VB to CB transition while the second one, centered at 330 nm, can only be attributed to a transition between the VB and localized states within the bandgap associated with defects, i.e. anionic vacancies or zinc in interstitial position for instance. The emission located at 440 nm can be associated with several radiative decay pathways. It may be due to transitions from shallow donor levels to the *2p*(O) levels or transitions from a deep donor levels to the VB. Finally, the emission located at 525 nm can be associated with transitions from localized levels associated with defects to the *2p*(O) states.

The effect of temperature on the emission was also investigated between 296 and 383 K using 270 nm excitation wavelength. As shown in Figure 8, the emission intensity of $ZnCN_2$ decreases by 47% between 293 and 383 K due to thermal quenching. Let us note that while the phenomenon appeared to be almost totally reversible, the initial emission intensity at RT was not fully recovered after thermal treatment at 383 K which can be attributed to a lower density of defects due to possible minor local rearrangements in the crystal structure.

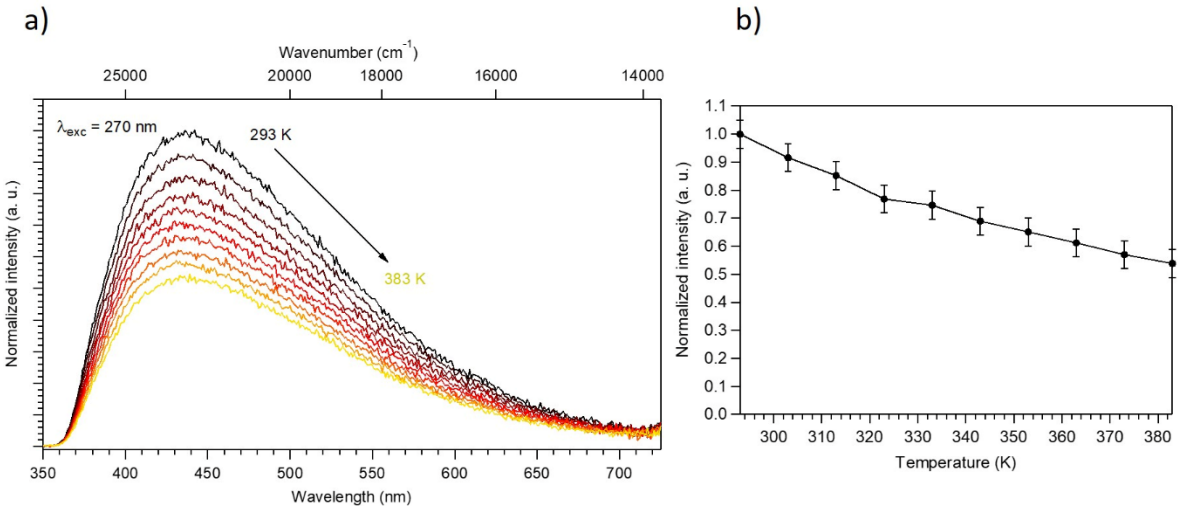

Figure 8. (a) Solid-state emission (λ_{ex} = 270 nm) spectra of $ZnCN_2$ at different temperature (296 - 393 K). (b) Normalized emission intensity (E_{max}) *vs* temperature (296 – 383 K) for $ZnCN_2$. Uncertainty bar = ±0.05.

3.3.2 Photoluminescence properties of Mn^{2+}-doped $ZnCN_2$ samples

The luminescence spectra of $Zn_{0.98}Mn_{0.02}CN_2$ at room temperature, the Commission Internationale de l'Eclairage (CIE) chromaticity diagram, chromaticity coordinates and picture under 254 nm UV lamp are presented in Figure 9. By monitoring the emission at 585 nm, the photoluminescence excitation spectra of $Zn_{0.98}Mn_{0.02}CN_2$ show several absorption bands. The high-energy stronger band around 270 nm corresponds to the host lattice excitation. The low-energy bands in the 350–500 nm wavelength region originate from the d–d transitions of Mn^{2+}; the intensities of these bands are weaker because the corresponding transitions are spin-forbidden. Excited by 270 nm light, the emission spectrum of $Zn_{0.98}Mn_{0.02}CN_2$ shows a broad emission band centered at about 585 nm with a full-width at half-maximum (FWHM) estimated around 66 nm. The broad emission band can be ascribed to the spin-forbidden transition of the Mn^{2+} ion from the $^4T_{1g}(^4G)$ lowest excited level to the $^6A_{1g}(^6S)$ ground state [30], and the CIE chromaticity coordinates are (x = 0.528, y = 0.452). The obtained decay time

value of this orange emission, calculated using a bi-exponential fitting model, is equal to 3.6(1) ms, which is typical for the parity and spin forbidden $^4T_{1g}(^4G) \rightarrow {}^6A_{1g}(^6S)$ transition of Mn^{2+} [31]. A secondary faster component (0.4(1) ms) is also observed indicating competitive de-excitation phenomena probably related to lattice defects (Figure S2). The presence of a unique broad emission band indicates that Mn^{2+} occupies only one site in the lattice, namely, the tetrahedrally coordinated Zn^{2+} site of the host lattice. This orange emission is in good agreement with those already observed in nitrides where the Mn^{2+} ion is also substituted for a divalent cation in tetrahedral site such as $MgSiN_2:Mn^{2+}$ or $ZnSiN_2:Mn^{2+}$ which have emission bands centered at 625 nm and 620 nm, respectively [15,16].

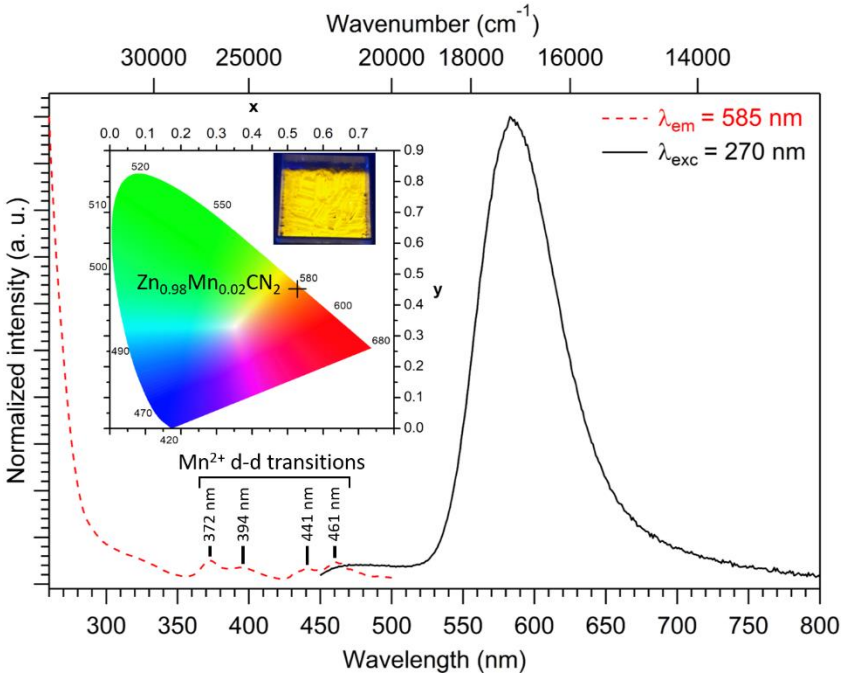

Figure 9. Solid-state excitation (λ_{em} = 585 nm) and emission (λ_{ex} = 270 nm) spectra at room temperature of $Zn_{0.98}Mn_{0.02}CN_2$. In inset: The CIE chromaticity diagram, chromaticity coordinates, and picture under 254 nm UV lamp.

Figure 10 shows the emission spectra of $Zn_{1-x}Mn_xCN_2$ (x = 0.005, 0.01, 0.02, 0.03, 0.04, 0.05 and 0.1) samples. Samples with doping rates between 0.5 and 2 mol% exhibit an additional emission band compared to samples with doping amounts greater than 2 mol%. This band between 450 nm and 530 nm is attributed to the luminescence related to defects states in the $ZnCN_2$ host lattice as previously discussed. The intensity of this band decreases with increasing the doping rate and the band disappears completely for Mn^{2+} contents greater than 2 mol%, which is attributed to energy transfer from the defect states to the excited states of Mn^{2+} ions as the activator concentration increases. In addition, while the shape and location of the red emission peaks do not vary with the Mn^{2+} doping concentration, the emission intensity strongly depends on it. The latter increases continuously ranging from 0.5 to 2 mol% and decreases from 2 to 10 mol%. Thus, the optimized Mn^{2+} doping concentration in $ZnCN_2$ host lattice is about 2 mol%. The reduction in emission intensity could be attributed to the concentration quenching effect arising mainly from non-radiative energy transfer between neighboring Mn^{2+} ions in $ZnCN_2$ host. Indeed, by increasing the concentration of the activators, the distances between them are reduced which results in increasing the probability of non-radiative energy transfers among the activators [32]. Let us note here, that the reduction of emission intensity of samples with a Mn^{2+} doping rate greater than 4 mol% could also be due to the presence of traces of $MnCN_2$ as secondary phase in the samples.

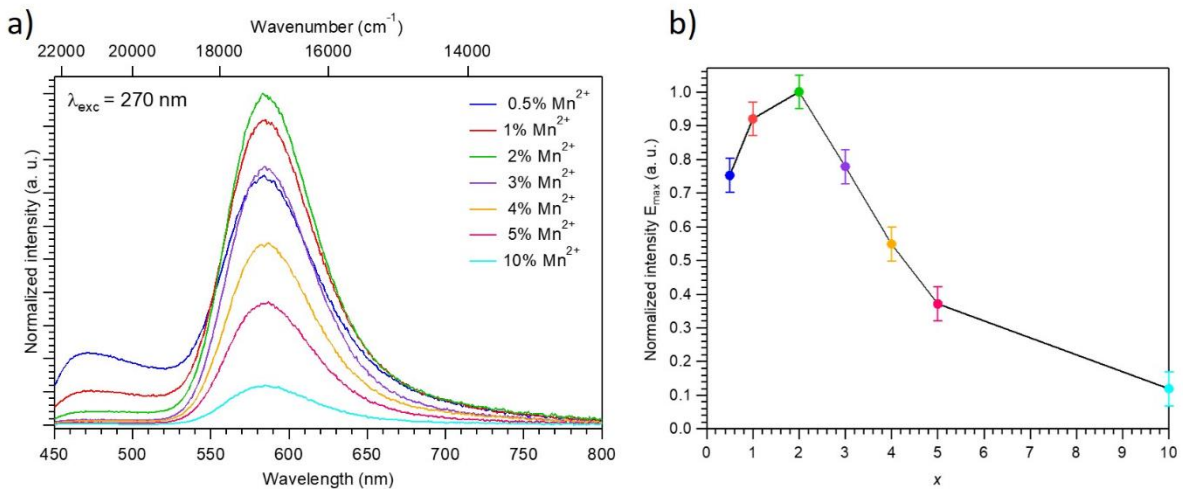

Figure 10. (a) Solid-state emission spectra at room temperature of $Zn_{1-x}Mn_xCN_2$ ($0 < x \leq 0.1$) samples (λ_{ex} = 270 nm). (b) Normalized emission intensity (E_{max}) vs *x* ($0 < x \leq 0.1$) for $Zn_{1-x}Mn_xCN_2$. Uncertainty bar = ±0.05.

The effect of temperature on emission was investigated between 293 and 385 K using 270 nm excitation wavelength. As shown in Figure 11, the emission intensity of $Zn_{0.98}Mn_{0.02}CN_2$ decreases drastically on the order of 90 % between 293 and 385 K. The temperature at which the emission intensity is reduced by 50% ($T_{1/2}$) is approximately 330 K. Let us note that the phenomenon is completely reversible indicating that the loss of luminescence is not due to any degradation of the product under the measurement conditions, which is in agreement with the thermal analyses which indicate a good thermal stability of $ZnCN_2$ under air up to 550°C (i.e. 823 K). The reduction of the emission intensity is consecutive to a higher probability of non-radiative transitions induced by higher temperature.

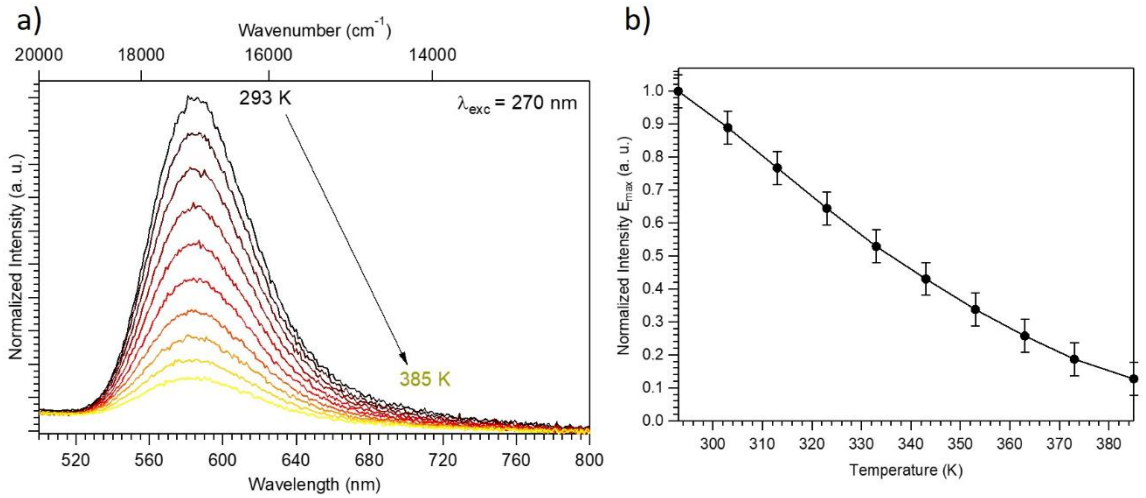

Figure 11. (a) Solid-state emission (λ_{ex} = 270 nm) spectra of $Zn_{0.98}Mn_{0.02}CN_2$ at variable temperature (296 - 393 K). (b) Normalized emission intensity (E_{max}) *vs* temperature (293 - 385 K) for $Zn_{0.98}Mn_{0.02}CN_2$. Uncertainty bar = ±0.05.

4. Conclusion

In this study, an alternative and cost-effective method to synthesize non-doped and Mn^{2+}-doped $ZnCN_2$ phosphors using carbon nitride as precursor has been successfully developed. X-ray diffraction results attested the formation of high-purity and well-crystallized $Zn_{1-x}Mn_xCN_2$ ($0 \leq x \leq 0.03$) samples. The

structural features of the as-prepared samples also indicate a maximum solubility of Mn^{2+} close to 3% within the investigated dopant concentration, with the insertion of Mn^{2+} within the host structure by substitution for the Zn^{2+} ions. Due to the large crystal-field effect induced by the coordinating nitrogen atoms, Mn^{2+} on tetrahedral site in $ZnCN_2$ exhibit a broad band emission with a peak centered at 585 nm at room temperature under 270 nm excitation wavelength. The optimized Mn^{2+} concentration of $ZnCN_2$:Mn^{2+} is 2 mol%. With increasing temperature, the emission intensity of $Zn_{0.98}Mn_{0.02}CN_2$ sample decreases drastically on the order of 90 % between 293 and 385 K. We also demonstrated that the non-doped $ZnCN_2$ host lattice exhibits photoluminescence properties with a blue emission at RT resulting from a broad band extending from 360 to 700 nm, with the presence of the energy band maximum at 440 nm and a shoulder at 525 nm. This photoluminescence has been ascribed to the presence of defects within the lattice (anionic vacancies, interstitial zinc atoms or oxygen defects). By analogy with the ZnO and ZnS systems and our experimental results, we proposed possible mechanisms that could be at the origin of the photoluminescence properties of the non-doped $ZnCN_2$.

Acknowledgements

SEM experiments were performed on CMEBA platform (ScanMAT, UMS 2011 University of Rennes 1-CNRS; CPER-FEDER 2007–2014). We also acknowledge Christophe Calers (ISCR, UMR 6226 University of Rennes 1-CNRS) for EDX measurements.

References

[1] J. Glaser, L. Unverfehrt, H. Bettentrup, G. Heymann, H. Huppertz, T. Jüstel, H.-J. Meyer, Crystal Structures, Phase-Transition, and Photoluminescence of Rare Earth Carbodiimides, Inorg. Chem. 47 (2008) 10455–10460. https://doi.org/10.1021/ic800985k.

[2] S. Yuan, Y. Yang, F. Cheviré, F. Tessier, X. Zhang, G. Chen, Photoluminescence of Eu^{2+}-Doped Strontium Cyanamide: A Novel Host Lattice for Eu^{2+}, J. Am. Ceram. Soc. 93 (2010) 3052–3055. https://doi.org/10.1111/j.1551-2916.2010.04025.x.

[3] E. Leysour de Rohello, Y. Suffren, O. Merdrignac-Conanec, O. Guillou, F. Cheviré, Effect of cationic substitutions on the photoluminescence properties of Eu^{2+} doped $SrCN_2$ prepared by a facile C3N4 based synthetic approach, J. Eur. Ceram. Soc. 40 (2020) 6316–6321. https://doi.org/10.1016/j.jeurceramsoc.2019.12.002.

[4] M. Krings, G. Montana, R. Dronskowski, C. Wickleder, α-SrNCN:Eu^{2+} − A Novel Efficient Orange-Emitting Phosphor, Chem. Mater. 23 (2011) 1694–1699. https://doi.org/10.1021/cm102262u.

[5] Y. Masubuchi, S. Nishitani, A. Hosono, Y. Kitagawa, J. Ueda, S. Tanabe, H. Yamane, M. Higuchi, S. Kikkawa, Red-emission over a wide range of wavelengths at various temperatures from tetragonal $BaCN_2$:Eu^{2+}, J. Mater. Chem. C. 6 (2018) 6370–6377. https://doi.org/10.1039/C8TC01289J.

[6] M. Kubus, C. Castro, D. Enseling, T. Jüstel, Room temperature red emitting carbodiimide compound $Ca(CN_2)$:Mn^{2+}, Opt. Mater. 59 (2016) 126–129. https://doi.org/10.1016/j.optmat.2016.01.006.

[7] E. Leysour de Rohello, Y. Suffren, O. Merdrignac-Conanec, O. Guillou, C. Calers, F. Cheviré, Synthesis and photoluminescence properties of Mn^{2+} doped $Ca_{1-x}SrxCN_2$ phosphors prepared by a carbon nitride based route, J. Solid State Chem. (2021) 122240. https://doi.org/10.1016/j.jssc.2021.122240.

[8] J. Sinko, Hybrid pigment grade corrosion inhibitor compositions and procedures, US6139610A, 2000. https://patents.google.com/patent/US6139610A/en.

[9] W. Zhao, J. Pan, F. Huang, Nonaqueous synthesis of metal cyanamide semiconductor nanocrystals for photocatalytic water oxidation, Chem. Commun. 54 (2018) 1575–1578. https://doi.org/10.1039/C7CC09699B.

[10] J.J. Arayamparambil, M. Mann, X. Liu, M. Alfredsson, R. Dronskowski, L. Stievano, M.T. Sougrati, Electrochemical Evaluation of Pb, Ag, and Zn Cyanamides/Carbodiimides, ACS Omega. 4 (2019) 4339–4347. https://doi.org/10.1021/acsomega.8b02748.

[11] M. Becker, M. Jansen, Zinc cyanamide, $Zn(CN_2)$, Acta Crystallogr. C. 57 (2001) 347–348. https://doi.org/10.1107/S0108270101000865.

[12] K. Morita, G. Mera, K. Yoshida, Y. Ikuhara, A. Klein, H.-J. Kleebe, R. Riedel, Thermal stability, morphology and electronic band gap of Zn(NCN), Solid State Sci. 23 (2013) 50–57. https://doi.org/10.1016/j.solidstatesciences.2013.06.008.

[13] K.M. Kaye, W. Grantham, G. Hyett, A Facile Route to Thin Films of Zinc Carbodiimide Using Aerosol-assisted CVD, Chem. Vap. Depos. 21 (2015) 281–287. https://doi.org/10.1002/cvde.201507179.

[14] N.J. Cherepy, S.A. Payne, N.M. Harvey, D. Åberg, Z.M. Seeley, K.S. Holliday, I.C. Tran, F. Zhou, H.P. Martinez, J.M. Demeyer, A.D. Drobshoff, A.M. Srivastava, S.J. Camardello, H.A. Comanzo, D.L. Schlagel, T.A. Lograsso, Red-emitting manganese-doped aluminum nitride phosphor, Opt. Mater. 54 (2016) 14–21. https://doi.org/10.1016/j.optmat.2016.02.008.

[15] K. Uheda, H. Takizawa, T. Endo, C. Miura, Y. Shimomura, N. Kijima, M. Shimada, Photo- and thermo-luminescence of zinc silicon nitride doped with divalent manganese, J. Mater. Sci. Lett. 20 (2001) 1753–1755. https://doi.org/10.1023/A:1012563812625.

[16] C.J. Duan, A.C.A. Delsing, H.T. Hintzen, Red emission from Mn^{2+} on a tetrahedral site in $MgSiN_2$, J. Lumin. 129 (2009) 645–649. https://doi.org/10.1016/j.jlumin.2009.01.010.

[17] Q.-H. Zhang, J. Wang, C.-W. Yeh, W.-C. Ke, R.-S. Liu, J.-K. Tang, M.-B. Xie, H.-B. Liang, Q. Su, Structure, composition, morphology, photoluminescence and cathodoluminescence properties of $ZnGeN_2$ and $ZnGeN_2$:Mn^{2+} for field emission displays, Acta Mater. 58 (2010) 6728–6735. https://doi.org/10.1016/j.actamat.2010.08.038.

[18] J. Rodríguez-Carvajal, Recent advances in magnetic structure determination by neutron powder diffraction, Phys. B Condens. Matter. 192 (1993) 55–69. https://doi.org/10.1016/0921-4526(93)90108-I.

[19] T. Roisnel, J. Rodríguez-Carvajal, WinPLOTR: A Windows tool for powder diffraction pattern analysis, Mater. Sci. Forum: Eur. Powder Diffraction EPDIC7 378–381, (2001) 118–123.

[20] J.-F. Bérar, P. Lelann, E.s.d.'s and estimated probable error obtained in Rietveld refinements with local correlations, J. Appl. Crystallogr. 24 (1991) 1–5. https://doi.org/10.1107/S0021889890008391.

[21] J.-F. Bérar, Data optimization and propagation of errors in powder diffraction, "Acc. Pow. Diff II", NIST sp. Pub 846 (1992), p. 63.

[22] D. Kubelka, L. Munk, Ein Beitrag zur Optik der Farbanstriche, Z. Tech. Phys. 12, (1931) 593–601.

[23] Crystallographic Open Database, http://www.crystallography.net.

[24] R.D. Shannon, Revised effective ionic radii and systematic studies of interatomic distances in halides and chalcogenides, Acta Crystallogr. A. 32 (1976) 751–767. https://doi.org/10.1107/S0567739476001551.

[25] V. Srikant, D.R. Clarke, On the optical band gap of zinc oxide, J. Appl. Phys. 83 (1998) 5447–5451. https://doi.org/10.1063/1.367375.

[26] A.K.R. Choudhury, 7 - Using instruments to quantify colour, in: A.K.R. Choudhury (Ed.), Princ. Colour Appear. Meas., Woodhead Publishing, 2014: pp. 270–317. https://doi.org/10.1533/9780857099242.270.

[27] S.A.M. Lima, F.A. Sigoli, M. Jafelicci Jr, M.R. Davolos, Luminescent properties and lattice defects correlation on zinc oxide, Int. J. Inorg. Mater. 3 (2001) 749–754. https://doi.org/10.1016/S1466-6049(01)00055-1.

[28] H. Zeng, G. Duan, Y. Li, S. Yang, X. Xu, W. Cai, Blue Luminescence of ZnO Nanoparticles Based on Non-Equilibrium Processes: Defect Origins and Emission Controls, Adv. Funct. Mater. 20 (2010) 561–572. https://doi.org/10.1002/adfm.200901884.

[29] J.-C. Lee, D.-H. Park, Self-defects properties of ZnS with sintering temperature, Mater. Lett. 57 (2003) 2872–2878. https://doi.org/10.1016/S0167-577X(02)01390-3.

[30] G. Blasse, B.C. Grabmaier, Luminescent Materials, Springer-Verlag, 1994. https://doi.org/10.1007/978-3-642-79017-1_1.

[31] L. Cornu, M. Duttine, M. Gaudon, V. Jubera, Luminescence switch of Mn-Doped $ZnAl_2O_4$ powder with temperature, J. Mater. Chem. C. 2 (2014) 9512–9522. https://doi.org/10.1039/C4TC01425A.

[32] D.L. Dexter, J.H. Schulman, Theory of Concentration Quenching in Inorganic Phosphors, J. Chem. Phys. 22 (1954) 1063. https://doi.org/10.1063/1.1740265.

Supporting information

Synthesis and photoluminescence properties of Mn^{2+} doped $ZnCN_2$ phosphors

Erwan Leysour de Rohello, Francesco Bour, Yan Suffren, Odile Merdrignac-Conanec, Olivier Guillou, François Cheviré*

Univ Rennes 1, INSA Rennes, CNRS, ISCR (Institut des Sciences chimiques de Rennes) – UMR 6226, F-35000 Rennes, France

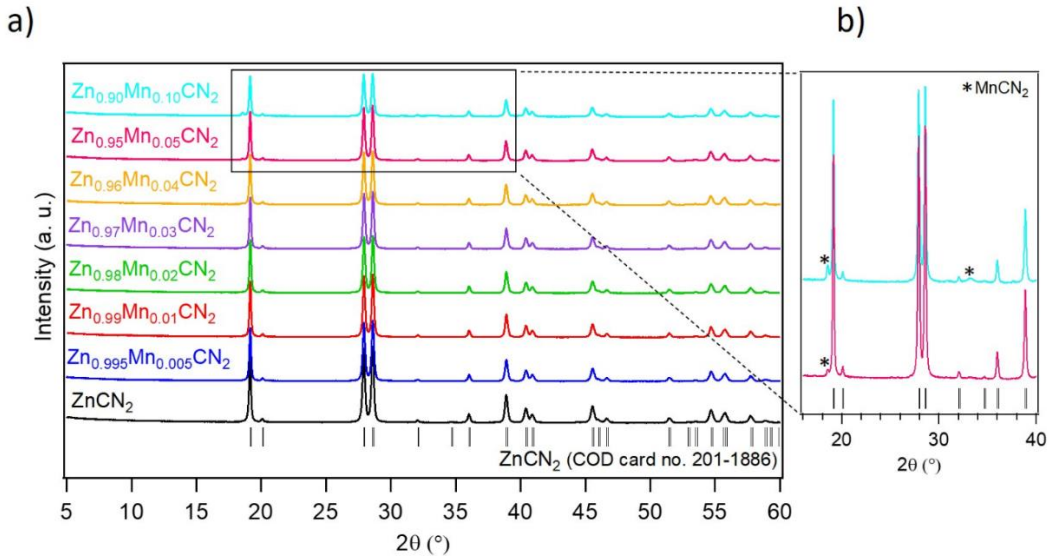

Figure S1. Powder X-ray diffraction diagrams of $Zn_{1-x}Mn_xCN_2$ ($0 \leq x \leq 0.1$) samples. Inset: Zoom on the X-ray diffraction diagrams of samples $Zn_{0.95}Mn_{0.05}CN_2$ and $Zn_{0.90}Mn_{0.10}CN_2$ between 18.5° and 33.2°

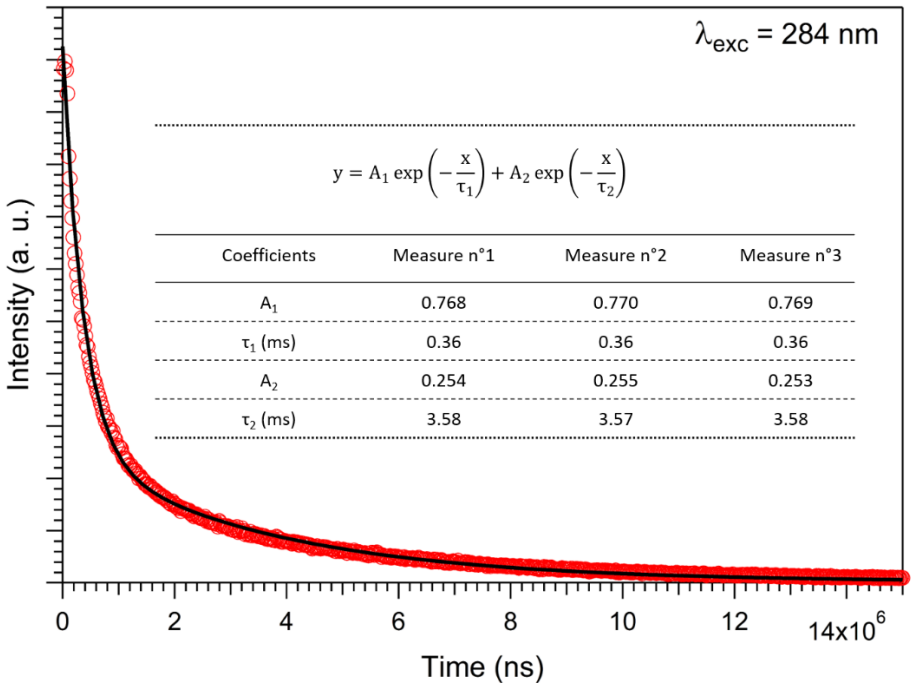

Coefficients	Measure n°1	Measure n°2	Measure n°3
A_1	0.768	0.770	0.769
τ_1 (ms)	0.36	0.36	0.36
A_2	0.254	0.255	0.253
τ_2 (ms)	3.58	3.57	3.58

Figure S2. Luminescent decay measurement of $Zn_{0.98}Mn_{0.02}CN_2$ at 300 K under photo-excitation at 284 nm.

Table S1. Occupied Wyckoff sites, refined atomic coordinates (in Å), isotropic atomic displacement parameters B_{iso} (in $Å^2$) and site occupancies of $Zn_{1-x}Mn_xCN_2$ samples (standard deviation in parentheses).

Atome	*Position*	*x*	*y*	*z*	B_{iso} ($Å^2$)	*Occupation*
			$ZnCN_2$			
Zn	*8d*	*0.9532(2)*	*0.25*	*0.125*	*0.81(5)*	*1*
C	*8d*	*0.75*	*0.066(1)*	*0.375*	*1.1(3)*	*1*
N	*16e*	*0.807(6)*	*0.071(6)*	*0.171(1)*	*0.4(1)*	*1*
			$Zn_{0.995}Mn_{0.005}CN_2$			
Zn	*8d*	*0.9531(2)*	*0.25*	*0.125*	*0.83(5)*	*0.995*
Mn	*8d*	*0.9531(2)*	*0.25*	*0.125*	*0.83(5)*	*0.005*
C	*8d*	*0.75*	*0.066(1)*	*0.375*	*1.1(3)*	*1*
N	*16e*	*0.808(6)*	*0.071(6)*	*0.171(1)*	*0.3(1)*	*1*
			$Zn_{0,99}Mn_{0,01}CN_2$			
Zn	*8d*	*0.9532(1)*	*0.25*	*0.125*	*0.78(4)*	*0.99*
Mn	*8d*	*0.9532(1)*	*0.25*	*0.125*	*0.78(4)*	*0.01*
C	*8d*	*0.75*	*0.0657(9)*	*0.375*	*0.9(2)*	*1*
N	*16e*	*0.8075(5)*	*0.0720(4)*	*0.1702(8)*	*0.3(1)*	*1*
			$Zn_{0.97}Mn_{0.03}CN_2$			
Zn	*8d*	*0.9534(1)*	*0.25*	*0.125*	*0.86(3)*	*0.97*
Mn	*8d*	*0.9534(1)*	*0.25*	*0.125*	*0.86(3)*	*0.03*
C	*8d*	*0.75*	*0.0671(8)*	*0.375*	*1.1(2)*	*1*
N	*16e*	*0.8075(5)*	*0.0744(4)*	*0.1697(8)*	*0.5(1)*	*1*
			$Zn_{0.96}Mn_{0.04}CN_2$			
Zn	*8d*	*0.9533(1)*	*0.25*	*0.125*	*0.84(4)*	*0.96*
Mn	*8d*	*0.9533(1)*	*0.25*	*0.125*	*0.84(4)*	*0.04*
C	*8d*	*0.75*	*0.0647(9)*	*0.375*	*1.1(2)*	*1*
N	*16e*	*0.8075(5)*	*0.0718(5)*	*0.1701(9)*	*0.4(1)*	*1*
			$Zn_{0.95}Mn_{0.05}CN_2$			
Zn	*8d*	*0.9534(1)*	*0.25*	*0.125*	*0.87(4)*	*0.95*
Mn	*8d*	*0.9534(1)*	*0.25*	*0.125*	*0.87(4)*	*0.05*
C	*8d*	*0.75*	*0.0660(9)*	*0.375*	*1.2(2)*	*1*
N	*16e*	*0.8068(5)*	*0.0716(5)*	*0.1714(8)*	*0.5(1)*	*1*
			$Zn_{0.90}Mn_{0.10}CN_2$			
Zn	*8d*	*0.9533(2)*	*0.25*	*0.125*	*0.73(7)*	*0.90*
Mn	*8d*	*0.9533(2)*	*0.25*	*0.125*	*0.73(7)*	*0.10*
C	*8d*	*0.75*	*0.0637(9)*	*0.375*	*1.0(4)*	*1*
N	*16e*	*0.807(1)*	*0.0720(8)*	*0.169(1)*	*0.4(2)*	*1*